

Development of Super Ensemble-based Aviation Turbulence Guidance (SEATG) for Air Traffic Management

Jung-Hoon Kim¹

Oak Ridge Associated Universities (ORAU) and NASA Ames Research Center, Moffett Field, CA

William N. Chan² and Banavar Sridhar³
NASA Ames Research Center, Moffett Field, CA

Robert D. Sharman⁴
The National Center for Atmospheric Research, Boulder, CO

A new method for forecasting turbulence is developed and evaluated using the high resolution weather model and *in situ* turbulence observations from commercial aircraft. The new method is an ensemble of various turbulence metrics from multiple time-lagged ensemble forecasts created using a sequence of four procedures. These include weather modeling, calculation of turbulence metrics, mapping the metrics into a common turbulence-scale, and production of final forecast. The new method uses similar methodology as current operational turbulence forecast with three improvements. First, it uses a higher resolution ($\Delta x = 3$ km) weather model to capture cloud-resolving scale phenomena. Second, it computes the metrics for multiple forecasts that are combined at the same valid time resulting in a time-lagged ensemble of multiple turbulence metrics. Finally, it provides both deterministic and probabilistic turbulence forecasts. Results show the new forecasts match well with observed radar reflectivity along a surface front as well as convectively induced turbulence outside the clouds on research period. Overall performance skill of the new turbulence forecast compared with the observed EDR data during the research period is superior to any single turbulence metric. The probabilistic turbulence forecast is used in an example air traffic management application for creating a wind-optimal route considering turbulence information. The wind-optimal route passing through areas of 50% potential for moderate-or-greater turbulence and the lateral turbulence avoidance routes starting from three different waypoints along the wind-optimal route from Los Angeles international airport to John F. Kennedy international airport are calculated using different turbulence forecasts. This example shows additional flight time is required to avoid potential turbulence encounters.

I. Introduction

Previous studies of wind-optimal routes and turbulence impacts to the National Airspace System have been conducted separately. This work aims to develop turbulence forecasts that can be used to evaluate how turbulence information affects wind-optimal routes. Previous work has not explicitly accounted for turbulence when applying to developing those routes though researchers have examined how pilots avoid areas of turbulence.

¹ NASA Post-doc (NPP) fellow, Aviation Systems Division, Mail Stop 210-10 (jung-hoon.kim@nasa.gov)

² Chief, Modeling and Optimization Branch, Mail Stop 210-8

³ Senior Scientist, Aviation Systems Division, Mail Stop 210-10

⁴ Project Scientist, Research Application Laboratory, P.O. Box 3000

To add turbulence information in the development of wind-optimal routes, the Super Ensemble-based Aviation Turbulence Guidance (SEATG) was developed. SEATG uses National Center for Atmospheric Research (NCAR)'s Graphic Turbulence Guidance (GTG; Sharman et al. 2006) methodology to create an ensemble of turbulence metrics that are then combined at the same forecast valid time using a time-lagged ensemble of previous forecasts. The use of time-lagged ensemble forecasts is not currently performed by the GTG but that technique does have benefits.

The following sections describe the background and methodology and procedures for creating SEATG forecasts. A comparison of SEATG forecasts with observed radar reflectivity and *in situ* EDR data will be also presented. Finally, as an example of a SEATG application to Air Traffic Management (ATM), wind-optimal routes are computed from Los Angeles International Airport (LAX) to John F. Kennedy International Airport (JFK) with and without a turbulence forecast.

II. Background

Several researchers have developed strategies for using wind-optimal routes for air traffic management. Ng et al. (2012) developed optimal flight trajectories that minimized flight time and fuel burn by computing minimum-time routes in winds on multiple flight levels. Palopo et al. (2010) conducted a simulation of wind-optimal routes and the impact on sector loading, conflicts, and airport arrival rates using a method developed by Jardin and Bryson (2001). Jardin and Bryson (2012) continued their research in this area by computing minimum-time flight trajectories using analytical neighboring wind-optimal routing in the presence of a strong jet with winds up to 160 knots. Prior research shows pilots seek to avoid areas of turbulence, and the impact of those maneuvers to air traffic management has been documented. Krozel et al. (2011) studied the maneuvers pilots made when they encountered Clear Air Turbulence (CAT). They showed the pilot's response to CAT depended on factors such as aircraft type and company policies. In that study, they looked at turbulence maneuvers for the next 50 miles of flight and found descending to be the quickest tactical solution. Ignoring CAT near a jet of strong winds to achieve minimum-time routes may result in flight and fuel savings that cannot be fully realized due to a pilot's unwillingness to traverse a turbulent area to reach the area of maximum tailwind. Research shows two-thirds of all severe CAT occurs near the jet stream (e.g., Lester 1994). Turbulence information can also aid in the development of routes around convective systems. Ng et al. (2009) calculated convective weather avoidance routes considering the probability of pilot deviation using a model based on radar data. The model used by Ng et al. (2009) and others to predict pilot behavior around convective systems, the Convective Weather Avoidance Model (CWAM), uses ground-based radar information to determine areas of convection where pilots will likely avoid (Delaura and Evans 2006). Such a model can miss regions of Convectively Induced Turbulence (CIT) outside the convective clouds. CWAM is currently used by NASA's Dynamic Weather Routing tool to create in-flight routing around convective weather and has been evaluated in field studies in collaboration with American Airlines (McNally et al. 2012).

To address the lack of turbulence information in those applications, SEATG extends current turbulence forecasting techniques by using time-lagged ensembles which has been shown to have some benefits. Steiner et al. (2010) completed a review of ensemble-based forecasting and state that ensemble forecasting can be applied to turbulence. They also state probabilistic forecasts are appropriate for strategic planning as they may provide guidance about the uncertainty associated with weather. In addition to using time-lagged ensemble forecasts for turbulence, SEATG also differs from GTG as it is based on a higher resolution numerical weather model. In addition,

SEATG creates both probabilistic and deterministic turbulence forecasts using several turbulence metrics based on the energy associated with turbulent eddies. These eddies result in bumpiness in flight for aircraft as they cascade down from larger scale disturbances into smaller spatial scales. SEATG forecasts these turbulence scales that are captured by the Eddy Dissipation Rate (EDR) which is defined as $\epsilon^{1/3}$ ($\text{m}^{2/3} \text{s}^{-1}$) and is an aircraft-independent atmospheric turbulence that can be mapped to aircraft turbulence. This forecasted EDR value is consistent with the observed *in situ* EDR metric, developed by NCAR, which has been deployed in several fleets of commercial airliners like B757s and B737s as an aircraft-independent atmospheric turbulence measurement (Cornman et al. 1995). The *in situ* EDR metric can be related to “light”, “moderate”, and “severe” aircraft turbulence and is the standard atmospheric turbulence unit required by the International Civil Aviation Organization (ICAO 2001) for routine turbulence reporting.

III. Methodology and Procedures of the SEATG Model

From a meteorological perspective, small-scale turbulent eddies that directly affect commercial aircraft at cruising altitudes are generated by a number of possible sources. For example, strong vertical shear above and below a jet stream core, inertial instability due to anticyclonic shear and curvature flow, and the gravity wave emissions via geostrophic adjustment in the jet stream exit region are well-known turbulence generation mechanisms near an upper-level jet/frontal system (e.g., Kim and Chun 2011). Mountain wave breaking frequently causes aviation turbulence over complex topographic regions (e.g., Sharman et al. 2012). Flow deformation, gravity wave breaking, and thermal-shear instability near the various convective systems are also considerable sources for aviation turbulence (e.g., Lane et al. 2012). To take into account several turbulence mechanisms and uncertainties in a turbulence forecast, a combination of several turbulence metrics due to different mechanisms and from different forecasts is essential, and is more reliable than using a single diagnostic or simple rule-of-thumb predictor (e.g., Kim et al. 2011). In addition, a high-resolution model uniformly covering a study area is more useful to forecast small-scale turbulence from an operational perspective.

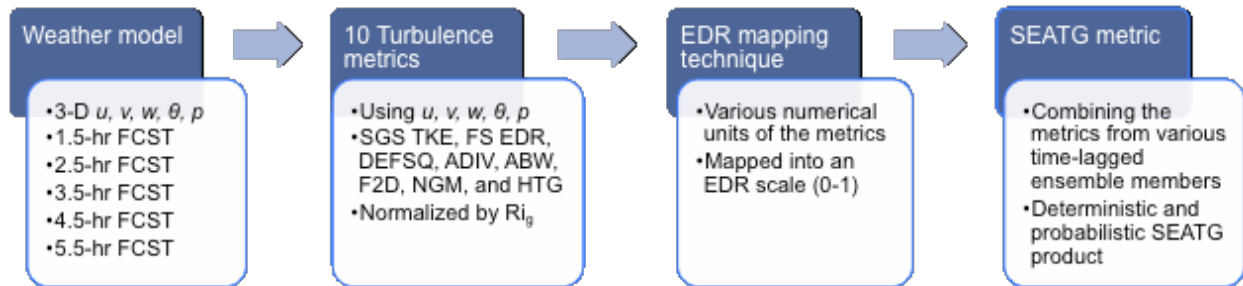


Fig. 1. Schematic chart of SEATG procedure.

SEATG is a sequence of four different processes as shown in the schematic chart in Fig. 1. The steps are summarized below followed with more detail.

- 1) A high-resolution weather model produces 3-dimensional meteorological data such as $u, v,$ and w wind components, potential temperature (θ), pressure (p), humidity, and cloud mixing ratios at the given valid time.

- 2) Ten aviation turbulence metrics for different turbulence generation mechanisms are calculated using meteorological data from the weather model.
- 3) The ten metrics from different time-lagged forecasts are mapped into a common atmospheric turbulence-scale (EDR-scale) based on log-normal (random) distribution theory of turbulence.
- 4) All EDR-scale metrics are combined to produce both deterministic and probabilistic turbulence forecasts.

1. Weather Model

In the first step, the Advanced Research Weather Research Forecast (WRF-ARW) model, developed through a community effort, is used as the weather model for SEATG. This model is a finite-difference implementation of the non-hydrostatic fully compressible prognostic equations on an Arakawa-C grid with terrain-following sigma vertical coordinates (Skamarock and Klemp 2008). In recent case studies of several turbulence encounters, WRF-ARW model simulations have successfully reproduced both the environmental weather scenario and the small-scale structures responsible for several turbulence events (e.g., Trier and Sharman 2009; Trier et al. 2010; Kim and Chun 2010; 2012). Horizontal domain size covering the entire Contiguous U.S. (CONUS) and the horizontal (3 km) and vertical grid spacings of the WRF-ARW model selected are the same ones used by the High Resolution Rapid Refresh (HRRR) operational system at National Oceanic and Atmospheric Administration (NOAA). Domain and terrain height in this model are shown in Fig. 2. The physical packages used in this WRF-ARW model, longest forecast time of each model run (6 hour), and frequency of model outputs (15 minutes) are also the same as the HRRR used by NOAA (<http://ruc.noaa.gov/hrrr/>). For the initial and boundary conditions, hourly reanalyses data that assimilate enhanced radar reflectivity over the CONUS are used from the 13-km Rapid Refresh (RAP) model. This WRF-ARW model was run using the Pleiades supercomputer at the NASA Ames Research Center (<http://www.nas.nasa.gov/hecc/>). Wall-clock run-time was one hour to complete one model run with 15-minute forecasts up to six hours using 500 cores.

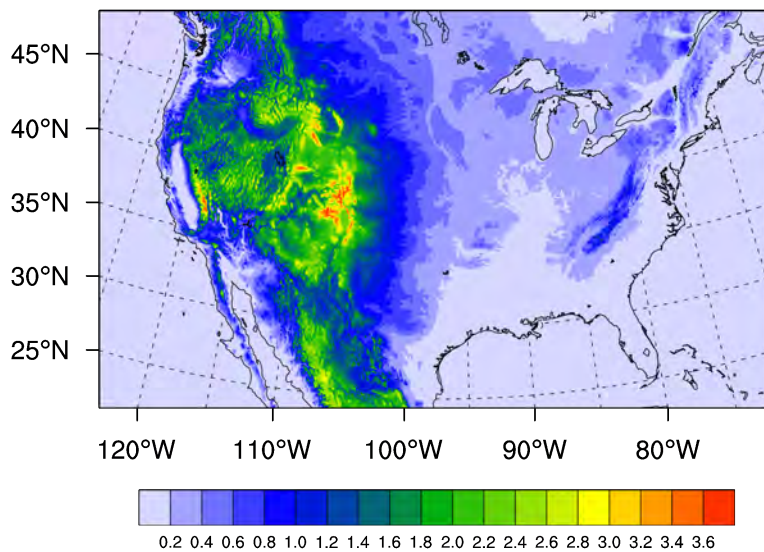


Fig. 2. Horizontal domain of WRF-ARW model for SEATG with terrain height (color shading showing red as higher than green that is higher than blue).

The following is a comparison of model forecasts against the observed meteorology for the study period. Figure 3 shows mosaic of observed radar reflectivity from the ground-based radar networks at 1730 UTC 7 Sep 2012. At this time, several convective clouds developed along a surface cold front elongated from the Great Lakes to Kansas. And, some of locally isolated convection clouds also developed ahead of the cold front along a squall line over Illinois and Indiana. Due to this convective system, several moderate-or-greater (MOG) turbulence events greater than 0.3 EDR value, scattered in the Northeastern CONUS, are observed by *in situ* EDR measurements from commercial aircraft (red dots in Fig. 4). Some of these EDR reports are located within the convective clouds, while others are outside of visible deep convection as confirmed by the radar data in Fig. 3. On 8 Sep 2012, as an upper-level trough deepened, clusters of thunderstorms along the eastward-moving cold front shown in Fig. 3 swept out the entire eastern and southern CONUS regions (not shown).

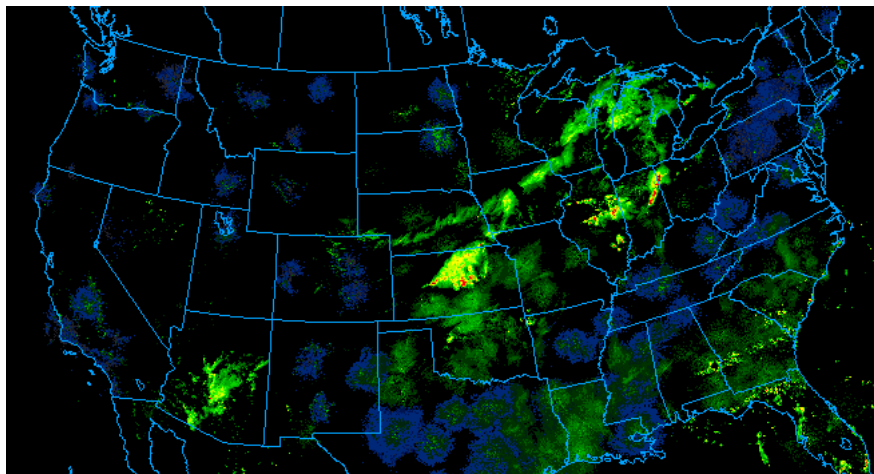


Fig. 3. Observed radar reflectivity (dBZ; shading in order of higher dBZ from blue green, yellow to red) at 1730 UTC 7 Sep 2012.

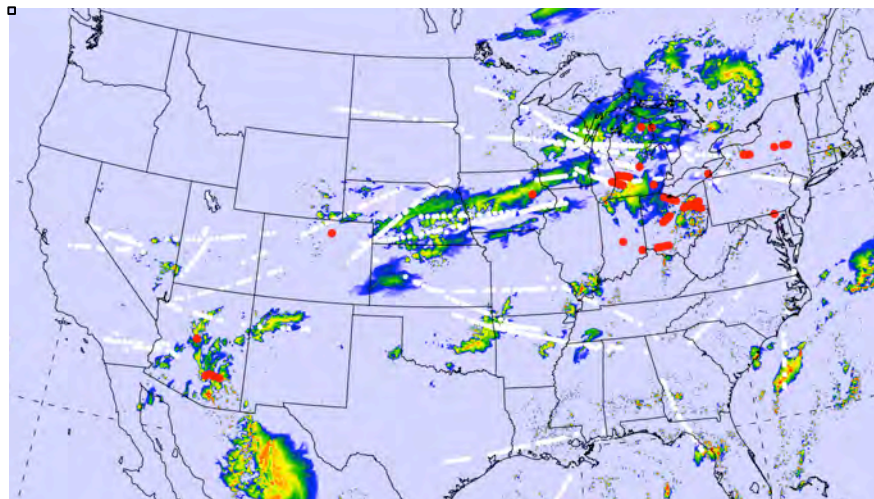


Fig. 4. Simulated maximum radar reflectivity (dBZ; shading in order of higher dBZ from blue green, yellow to red) derived from 2.5-hr forecast data with null (white dots) and MOG (red dots) *in situ* EDR observations at 1730 UTC 7 Sep 2012.

These radar observations are reasonably well captured by the WRF-ARW model. In particular, forecasted radar echoes along an elongated front from the Great Lakes to Kansas in Fig. 4 are qualitatively well matched with the observed radar data in Fig. 3. This gives confidence that the large-scale flow-generated convective clouds responsible for aircraft-scale turbulence are well reproduced by ARW-WRF model in SEATG. Considering that the upper-level westerly jet stream is dominant during this period over the northeastern CONUS (see Figs. 8 and 9), turbulence scattered in this area may also be generated either by a deep convection-induced disturbance or jet stream-related instabilities. Due to the multiple turbulence-causing mechanisms, combinations of turbulence metrics based on various turbulence generation mechanisms are essential to accurately forecast turbulence events.

2. Ten Turbulence Metrics

For the second step, ten turbulence metrics were computed. Although the horizontal grid spacing of 3 km was used in the WRF-ARW model, the horizontal size of aircraft-scale turbulence (normally 10-1,000 m) is still smaller (i.e., subgrid-scale). However, aircraft-scale turbulence can be diagnosed by assuming that small-scale turbulent eddies directly affecting commercial aircraft cascade down from large-scale (resolved scale) disturbances revealed as high values of the turbulence metrics (e.g., Lindborg 2007). In this study, up to five different weather forecasts (e.g., 1.5-5.5 hr forecast lead times) were used to calculate the turbulence metrics for each valid time. Upper-level turbulence metrics selected have the high performance skills in the operational GTG system (Sharman 2013). The ten turbulence metrics used are the WRF-produced subgrid-scale turbulent kinetic energy (SGS TKE), Frehlich and Sharman's EDR (FS EDR), square of total deformation (DEFSQ), absolute value of horizontal divergence (ADIV), square of vertical component of relative vorticity (VORTSQ), absolute value of vertical velocity (ABW), two-dimensional frontogenesis function on pressure coordinate (F2D), Brown turbulence index 1 (Brown1), nested grid model turbulence index (NGM), and the horizontal temperature gradient (HTG). Detailed descriptions of these are provided in Appendix A. These metrics were then normalized by the gradient Richardson number (Ri_g), as previous work shows this improves the performance skills of turbulence forecast metrics against observed turbulence reports from both PIREPs and *in situ* EDRs (Sharman 2013).

$$Ri_g(x, y, z) = \frac{N^2(x, y, z)}{S^2(x, y, z)}, \quad (1)$$

$$N^2(x, y, z) = \frac{g}{\theta(x, y, z)} \frac{\partial \theta(x, y, z)}{\partial z}, \quad (2)$$

$$S^2(x, y, z) = \left[\frac{\partial U(x, y, z)}{\partial z} \right]^2 + \left[\frac{\partial V(x, y, z)}{\partial z} \right]^2. \quad (3)$$

Here, U and V are grid-scale horizontal wind components along x and y directions, and θ is potential temperature. N is the buoyancy (Brunt-Väisälä) frequency and S is the vertical wind shear. Within a given grid point, areas with smaller background Ri_g are more vulnerable for aircraft-scale turbulence due to any kind of subgrid-scale forcing and/or triggers diagnosed by various turbulence metrics in the upper troposphere and lower stratosphere (UTLS) where the atmosphere is mostly statically stratified.

3. EDR Mapping Technique

This third step describes how different turbulence diagnostics from separate forecasts are mapped onto a common atmospheric turbulence scale. The previously described turbulence metrics have different numerical formulations and units. However, a final turbulence forecast should be on a common scale such as the EDR. EDR is independent to aircraft type or size and mapping turbulence metrics into the EDR scale allows them to be compared with observed *in situ* EDR measurements. So, all of the turbulence metrics calculated were mapped into the EDR scale. In this study, the GTG methodology is used by assuming that the model-derived turbulence metrics have their own log-normal distributions that are consistent with the best fit function of the observed *in situ* EDR distribution especially for larger values of turbulence metrics (Sharman 2013). Figure 5 shows an example of nine EDR-scale turbulence metrics from a 2.5-hr forecast product averaged at three different levels at FL300, FL350, and FL400 valid at 1730 UTC 7 Sep 2012. In general, most of the EDR-scale metrics for both null (smaller than $0.1 \text{ m}^{2/3} \text{ s}^{-1}$) and MOG-level (higher than $0.3 \text{ m}^{2/3} \text{ s}^{-1}$) turbulence events are well matched with null (gray dots) and MOG (blue dots) of the observed *in situ* EDR events.

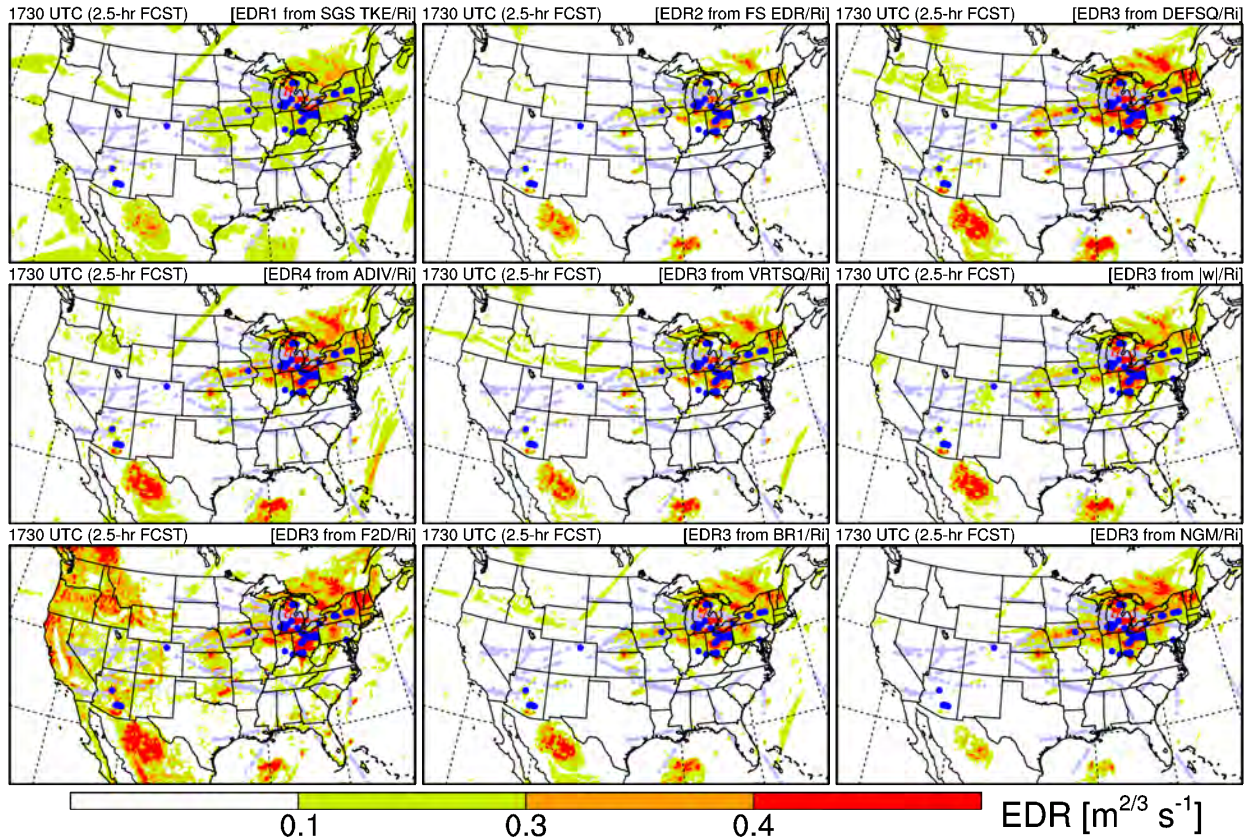


Fig. 5. An example of snapshots of nine EDR-scale turbulence metrics (SGS TKE/Ri, FS EDR/Ri, DEFSQ/Ri, ADIV/Ri, VRTSQ/Ri, $|w|/Ri$, F2D/Ri, BR1/Ri, NGM/Ri) derived from 2.5-hr forecast data of WRF-ARW model averaged three layers of FL300, FL350, and FL400 valid at 1730 UTC 7 Sep 2012. Observed *in situ* EDR locations are also depicted as gray (null intensity) and blue (MOG intensity) dots in all plots.

4. SEATG Metric

This final step combines all EDR-scale metrics into deterministic and probabilistic turbulence forecasts. At a given forecast time, eventually up to a total 50 of EDR-scale turbulence metrics [i.e., ten different turbulence metrics from five different weather forecasts (1.5-5.5 hr forecast data)] can be used for the ensemble EDR forecasts as well as SEATG. These three-dimensional turbulence metrics are combined into a three-dimensional ensemble EDR forecast or deterministic SEATG using a simple averaging methodology, as follows.

$$\text{Ensemble EDR}(x, y, z) = \left\{ \sum_{i=1}^N \text{EDR}_i(x, y, z) \right\} / N, \quad i = 1, 2, 3, \dots, N. \quad (4)$$

A probabilistic turbulence forecast product takes into account the uncertainties of weather. In this study, the probabilistic turbulence product is calculated by evaluating how many turbulence metrics at a given grid point have higher EDR values for corresponding turbulence intensity of moderate (MOD; $0.3 \text{ m}^{2/3} \text{ s}^{-1}$) and severe (SEV; $0.4 \text{ m}^{2/3} \text{ s}^{-1}$). Figure 6 shows a snapshot of a deterministic forecast using Eq. (4) (left) and a probabilistic forecast for MOG-level turbulence (right). These are averaged from flight levels FL300, FL350, and FL400 using three time-lagged ensemble members of forecast data (2.5-4.5 hr) valid on 1730 UTC Sep 2012. Results show the deterministic EDR-scale forecast for greater than $0.3 \text{ m}^{2/3} \text{ s}^{-1}$ mostly agrees well with MOG-level observed *in situ* EDR measurements (blue dots and asterisks) in Fig. 6 (left). For the probabilistic forecast, 30% of MOG-level forecasted turbulence potential is also consistent with MOG-level observations (blue dots and asterisks) especially located over western Michigan and northern Ohio shown in Fig. 6 (right). Considering that the background (natural) probability for MOG-level turbulence encounters in UTLS is less than 2%, the forecasted MOG-level turbulence potential in Fig. 6 (right) is regarded as significantly large probabilities of MOG-level turbulence potentials in UTLS (Sharman et al. 2006; Sharman 2013).

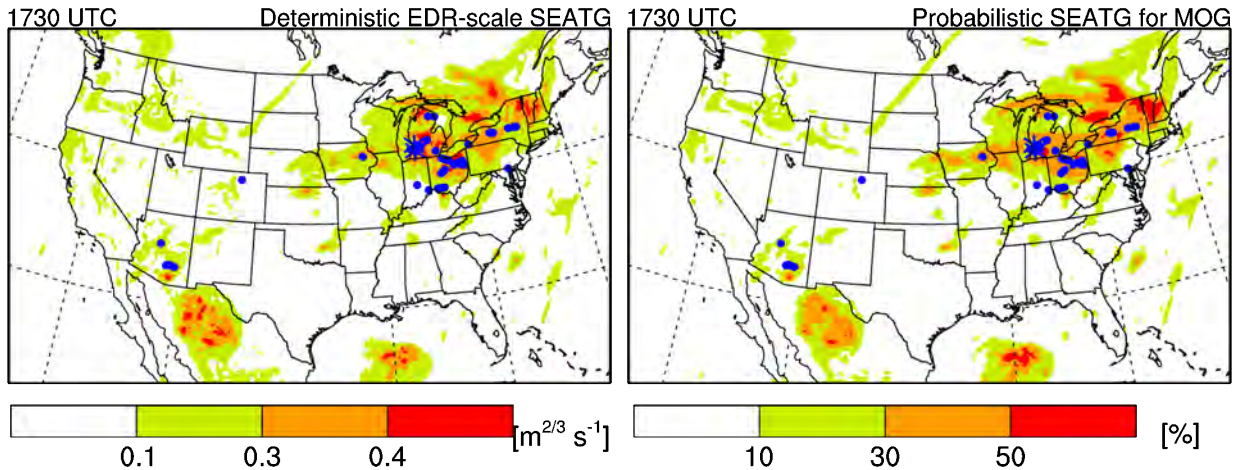


Fig. 6. Deterministic EDR-scale forecast (left) and probabilistic forecast for MOG-level turbulence (right) averaged using three layers of FL300, FL350, and FL400 using 2.5-4.5 hr time-lagged weather forecasts valid at 1730 UTC 7 Sep 2012. Observed *in situ* EDR measurements for MOD (blue dots) and SEV (blue asterisks) intensities are also depicted in the plots. Note that the color shadings in each plot are different.

IV. Evaluations of EDR-scale SEATG and Turbulence Metrics

In this section, the forecasted EDR-scale turbulence metrics shown in Fig. 5 and deterministic SEATG shown in Fig. 6 (left) are compared with *in situ* EDR observations to obtain the skill for the forecasted turbulence metrics. In this study, the forecasting performance skills are calculated using the probability-of-detection “yes” (PODY) for MOG and “no” (PODN) for null observations, used for the validation of various turbulence forecasts (e.g., Sharman et al. 2006; Kim et al. 2011). If the forecasted value of each EDR-scale ensemble or turbulence metric at the nearest grid point of the observed MOG location around ± 30 minutes (30 minute time window) at the valid time is higher (lower) than the given threshold of observed *in situ* EDR, the $Y_{for}Y_{obs}$ ($N_{for}Y_{obs}$) was counted as shown in Table 1. On the other hand, if the forecasted EDR value near the null observation is smaller (higher) than the given threshold of observed *in situ* EDR, the $N_{for}N_{obs}$ ($Y_{for}N_{obs}$) was counted. These procedures were applied to a total of 1,018 MOG and 36,039 null events on 7-8 Sep 2012. Then, this process was repeated through 20 different thresholds that ranged from EDR values of 0 to 1, resulting in 20 PODY and PODN statistics for both the EDR-scale SEATG and turbulence metrics.

Table 1. 2×2 contingency table for probability-of-detection (POD) statistics methodology.

Forecast (for)	Observation (obs)	
	Yes	No
Yes	$Y_{for}Y_{obs}$	$Y_{for}N_{obs}$
No	$N_{for}Y_{obs}$	$N_{for}N_{obs}$

$$PODY = \frac{Y_{for}Y_{obs}}{Y_{for}Y_{obs} + N_{for}Y_{obs}}, \text{ and } PODN = \frac{N_{for}N_{obs}}{Y_{for}N_{obs} + N_{for}N_{obs}}. \quad (5)$$

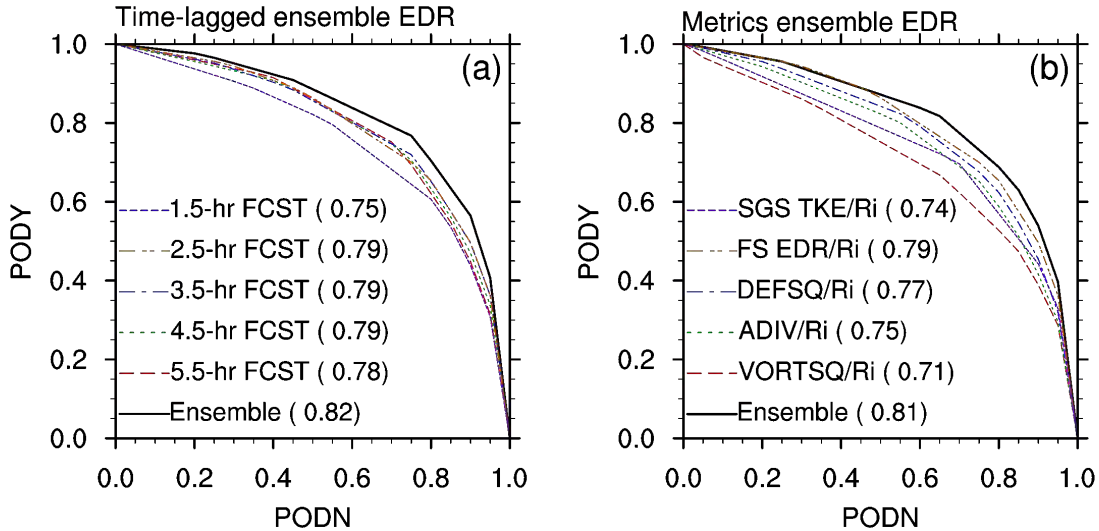


Fig. 7. PODY and PODN statistics of (a) FS EDR/Ri EDR metrics from 1.5-hr (purple dashed line), 2.5-hr (orange dash-dot-dotted line), 3.5-hr (blue dash-dotted line), 4.5-hr (green dotted line), and 5.5-hr (red long dashed line) forecast data and time-lagged ensemble (black bold-solid line) EDR and (b) EDR-scale turbulence metrics (SGS TKE/Ri; purple dashed line, FS EDR/Ri; orange dash-dot-dotted line, DEFSQ/Ri; blue dash-dotted line, ADIV/Ri; green dotted line, VORTSQ/Ri; red long dashed line) from 2.5-hr forecast data and ensemble metric EDR (black bold-solid line) compared with the observed *in situ* EDR measurements for 7-8 Sep 2012.

Figure 7a shows the x - y plot of these 20 PODY and PODN statistics for the FS EDR/Ri turbulence metrics against total of the null and MOG events on 7-8 Sep 2012 as a function of different forecast lead times (1.5-5.5 hr). Values of area under the curve (AUC) for 20 PODY and PODN statistics are the forecast performance skills for turbulence metrics. An AUC = 1 is a perfect forecast [i.e., a turbulence metric can perfectly discriminate all MOG and null turbulence events and/or a turbulence metric has a perfect forecast for MOG turbulence without any false alarms (1-PODN)]. Using Eq. (4) described in the previous section, a time-lagged ensemble for the FS EDR/Ri metric was calculated by combining the FS EDR/Ri metrics from three different weather forecasts (between 2.5-4.5 hr forecasts). In Fig. 7a, combining them (black bold line) results in higher forecasting performance skill (0.82) than a single FS EDR/Ri turbulence metric from one specific weather forecast. Figure 7b shows an example of PODY and PODN statistics with their AUC values for SGS TKE/Ri, FS EDR/Ri, DEFSQ/Ri, ADIV/Ri, and VORTSQ/Ri derived from the 2.5-hr forecasts against all of the null and MOG *in situ* EDR observations during 7-8 Sep 2012. As in Fig. 7a, when the metrics-ensemble EDR was computed using ten turbulence metrics from a specific weather forecast (i.e., 2.5-4.5 hr forecast lead time in Fig. 7b), its performance skill (black bold line; 0.81) is also higher than any single metric in Fig. 7b.

Table 2. AUC (area under the curve) values for ten turbulence EDR metrics and time-lagged ensemble EDR metrics from different weather forecasts (1.5-5.5 hr forecast) and time-lagged ensemble of 2.5-4.5 hr forecasts. AUC for the deterministic SEATG is 0.83 (bold).

Metrics	1.5-hr	2.5-hr	3.5-hr	4.5-hr	5.5-hr	Time-Lagged Ensemble
SGS TKE/Ri	0.73	0.74	0.73	0.72	0.72	0.76
FS EDR/Ri	0.75	0.79	0.79	0.79	0.78	0.82
DEFSQ/Ri	0.75	0.77	0.76	0.76	0.76	0.81
ADIV/Ri	0.74	0.75	0.74	0.74	0.74	0.79
VORTSQ/Ri	0.67	0.71	0.70	0.71	0.70	0.77
$ w /Ri$	0.72	0.74	0.73	0.73	0.73	0.79
F2D/Ri	0.70	0.72	0.71	0.71	0.71	0.77
Brown1/Ri	0.76	0.78	0.77	0.76	0.76	0.81
NGM/Ri	0.79	0.80	0.79	0.79	0.79	0.82
HTG/Ri	0.69	0.71	0.70	0.70	0.70	0.74
Metric Ensemble	0.80	0.81	0.81	0.80	0.80	0.83

All of the AUC values for the ten turbulence metrics from different weather forecasts (1.5-5.5 hr forecasts) as well as for both time-lagged ensemble EDRs (rightmost column) and metrics ensemble EDRs (lowermost row) are also shown in Table 2. In general, all of the turbulence metrics have the best performance for the 2.5-hr forecast. As forecast-lead time increases from 1.5-hr to 2.5-hr, the forecast skill improves due to model spin-up time required to build the convective storms along the elongated cold frontal system. The skill is slightly reduced as the forecast-lead time increases from 2.5-hr to 5.5-hr. Eventually, the AUC value of deterministic SEATG forecast was calculated using both the time-lagged ensemble forecast and an ensemble of the turbulence metrics (i.e., ensemble of ensemble or super ensemble), which in turn has the best turbulence forecasting skill (AUC = 0.83 in Table 2) verified against observed *in situ* EDR

measurements for 7-8 Sep 2012. This is consistent with the previous results of turbulence forecasts that the integrated turbulence metrics are always superior in forecasting skill than any single turbulence metric (e.g., Sharman et al. 2006; Kim et al. 2011; Gill 2012; Gill and Stirling 2012).

V. Example of SEATG Application to ATM

In this study, an example wind-optimal route (WOR) considering probabilistic SEATG turbulence forecasts is presented to illustrate the use of this information to develop two simple lateral turbulence avoidance routes (LTARs). With a correct choice of initial heading angle, the minimum-time path in the presence of wind can be obtained by applying Pontryagin's Minimum Principle to determine the analytic solution for the control parameter (i.e., the heading angle of cruising aircraft) in the governing equations of the simplified horizontal aircraft motions on sphere of Earth, as follows (e.g., Hok et al. 2011).

$$\frac{d\phi(t)}{dt} = \frac{V_a \cos\psi(t) + U(\phi, \theta, z)}{R \cos\theta(t)}, \quad (6)$$

$$\frac{d\theta(t)}{dt} = \frac{V_a \sin\psi(t) + V(\phi, \theta, z)}{R}, \quad (7)$$

$$\frac{d\psi(t)}{dt} = -\frac{F_{wind}(t)}{R \cos\theta(t)}. \quad (8)$$

Here, ϕ , θ , ψ are longitude, latitude, and heading angle of aircraft, and U and V are u and v wind components, respectively. R is the Earth's radius that Earth is assumed to be a sphere and $R \gg z$, and V_a is the cruising speed of aircraft that is 250 m s^{-1} . Full derivation of analytic solution for control parameter (ψ) including $F_{wind}(t)$ is described in Appendix B.

$$\alpha(t + 1) = \alpha(t) + \Delta t \frac{d\alpha(t)}{dt}, \text{ where } \alpha = \phi, \theta, \text{ and } \psi. \quad (9)$$

Integration of Eqs. (6), (7), and (8) was then conducted using an explicit Euler forward integration scheme (9) from LAX [$\phi(t_0)$, $\theta(t_0)$, $\psi(t_0)$] with $\Delta t = 60$ seconds until the great circle distance between a waypoint of trajectory and JFK [$\phi(t_f)$, $\theta(t_f)$, $\psi(t_f)$] is minimized.

In this study, to select the optimal initial heading angle, the integration of each trajectory with different initial heading angles were iterated 90 times with a total of 90 initial heading angles that ranged from $\psi_{GC} - 22.5^\circ$ to $\psi_{GC} + 22.5^\circ$ with 0.5° increments, where the ψ_{GC} is great circle heading angle between LAX and JFK. Finally, the closest trajectory passing through JFK [$\phi(t_f)$, $\theta(t_f)$, $\psi(t_f)$] is regarded as the WOR from LAX to JFK at FL350. The WOR is shown as blue line in Fig. 8.

$$J = \int_{t_0}^{t_f} \{C_t + C_r r(\phi, \theta, z)\} dt. \quad (10)$$

LTAR can be optimized by determining the heading angle that minimizes a cost function (J). Here, C_t and C_r are the cost coefficients of travel time and penalty areas through forecasted turbulence areas along the trajectory, respectively. In this study, $r(\phi, \theta, z) = 1$ when the

probabilistic SEATG forecast for MOG-level turbulence is higher than 50%, and elsewhere $r(\phi, \theta, z) = 0$ (e.g., Sridhar et al. 2010; Hok et al. 2011). Eventually, an analytic solution for heading angle of the LTAR is obtained, as follows:

$$\frac{d\psi(t)}{dt} = -\frac{\{F_{wind}(t) + F_{turb}(t)\}}{R \cos\theta(t) \{C_t + C_r r(\phi, \theta, z)\}} \quad (11)$$

Full derivation of this, including $F_{turb}(t)$, is in Appendix B. Similar to the WOR, the LTAR also uses the great circle (ψ_{GC}) heading angle as the first guess of the initial heading angle. Following this, routes starting from LAX using 90 extremal trajectories with different initial heading angles were calculated by integrating Eqs. (6), (7), and (11) using Eq. (9). Finally, the LTAR that passes nearest to destination (i.e., JFK) is regarded as the best LTAR in this study.

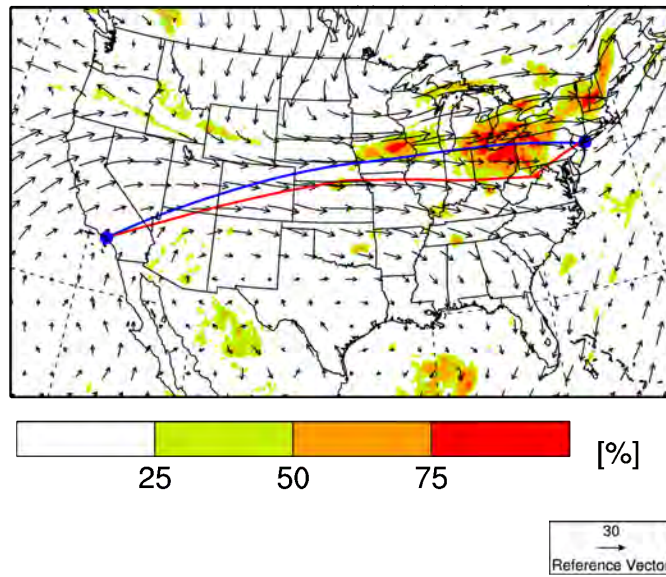


Fig. 8. Probabilistic SEATG forecast for MOG-level turbulence with horizontal wind vectors and Wind-Optimal Route (WOR; blue line) and Lateral Turbulence Avoidance Route (LTAR; red line) at FL350 from Los Angeles (LAX) to John F. Kennedy (JFK) international airports using 3.5-5.5 hr forecasts valid at 1730 UTC 9 Sep 2010. For the magnitude of wind speed, reference vector for 30 m s^{-1} of horizontal wind speed is depicted on the right bottom of the plot.

In Fig. 8, LTAR trajectory for 50% MOG-level turbulence using 3.5-5.5 hr forecasts is depicted as a red line. Consequently, for 50% of MOG-level forecasted turbulence in Fig. 8, the flight time for the WOR (blue line) takes 238 minutes where 56 minutes of that time was in MOG-level forecasted turbulence areas. The LTAR (red line) takes total of 254 minutes flying time and used 6.7% more fuel to entirely avoid forecasted 50% MOG-level turbulence areas. Note that this LTAR shown in Fig. 9 would not be the best efficient maneuver as there are several other ways to avoid the potential constraints of turbulence such as tactical change of flight altitude and route just ahead of turbulence areas. Additionally, this LTAR is initiated from LAX which is not as preferable to delaying such a maneuver until closer to the forecasted turbulence constraint, because the maneuver decision needs to consider several factors like air-capacity reduction and confidence of the weather forecast. Delaying the maneuver is shown in the following routing examples.

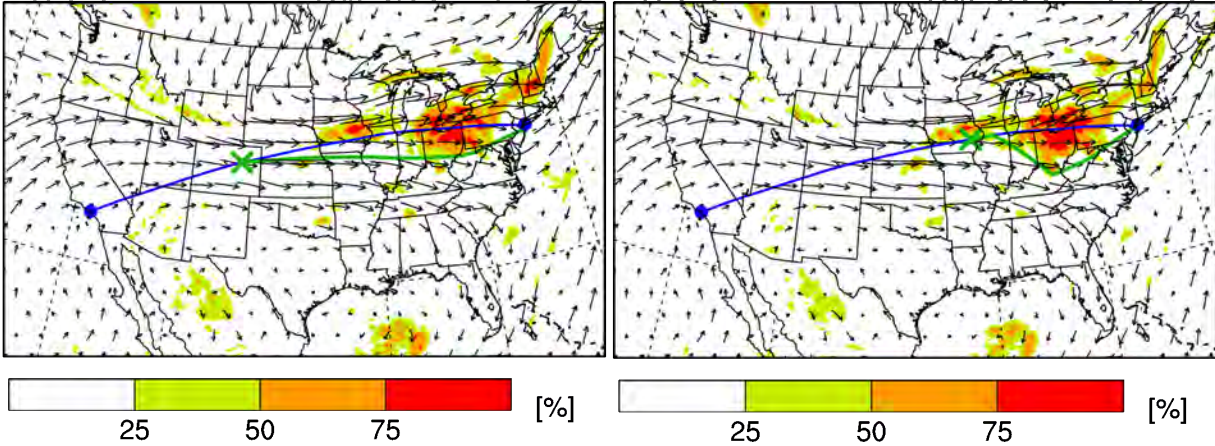


Fig. 9. The same as Fig. 8 except for the LTARs (green lines) initiated after 1.5-hr (left) and 2.5-hr (right) departing from LAX along the WOR (blue lines) between LAX to JFK using 2.5-4.5 hr forecasts (left) and using 1.5-3.5 hr forecasts (right) valid at 1730 UTC 9 Sep 2010.

Two other alternative LTARs that initiated 1.5 hrs (left) and 2.5 hrs (right) after departing LAX along the WOR (blue lines) shown in Fig. 9 are shown as an example of delaying the maneuver to account for uncertainties of the weather. An aircraft that follows the LTAR 1.5 hrs after departing LAX (left in Fig. 9) has a flying time of 244 minutes, which saves 10 minutes more than that if it were to follow the LTAR shown in Fig. 8. However, if an aircraft follows an LTAR 2.5 hrs after departing LAX, when it is closer to more recently forecasted regions (right in Fig. 9), it takes total of 256 minutes of flying time. This is 2 minutes even longer than the LTAR shown in Fig. 8. Alternatively, a vertical deviation could have been used instead if that may result in less fuel used.

VI. Summary and Conclusions

In this paper, the development of a higher resolution super ensemble turbulence system is described with an example application for routing around turbulence constraints in the CONUS. The SEATG system can create both a deterministic and probabilistic turbulence forecast using a sequence of four procedures. These include high-resolution weather modeling, calculation of ten turbulence metrics, mapping of these metrics to an EDR-scale, and combining the predictions of these ten metrics into a forecast SEATG product. This system is directly motivated by and modified upon the operational Graphic Turbulence Guidance (GTG), which we believe will give improved performance. One modification is a finer horizontal grid, and the second is the development of a super ensemble (i.e., time-lagged ensemble forecast with an ensemble of various turbulence metrics). Third is the probabilistic turbulence information. The developed SEATG turbulence forecast was created and evaluated for 7-8 Sep 2012 when several convective clouds developed along the surface frontal system and swept the mid and eastern CONUS. The deterministic version of the turbulence forecast was verified against observed *in situ* turbulence measurements. The SEATG was observed to have a higher forecasting performance than other ensemble EDRs as well as any single turbulence metric. Probabilistic SEATG forecast information is used for the ATM decision.

A simple Wind-Optimal Route (WOR) was developed to show the utility of this forecast product for defining more operationally useful WOR. Using the WOR and ignoring any

turbulence maneuvers, an aircraft was modeled to encounter MOG-level turbulence for 56 minutes but to laterally detour around these potential areas of the turbulence from the departure airport (LAX) an aircraft would incur 16 minutes (6.7%) more travel time to fly to its destination (JFK). Delaying the horizontal maneuver would result in either a savings of 10 minutes if the maneuver was delayed 1.5 hrs after leaving LAX or an extra 2 minutes if the maneuver was delayed by 2.5 hrs.

Future work includes exploring other alternate time-synchronized routing algorithm and application of the SEATG methodology to create forecasted turbulence regions, which can be avoided. Practical considerations include reducing the SEATG run-time, which would make SEATG useful for more tactical decisions such as near-term routing around convective weather. This can be accomplished by using data from a nowcast version of the GTG or output from a faster-running numerical model.

Acknowledgments

This work was supported by an appointment to the NASA Postdoctoral Program at the Ames Research Center, administrated by the Oak Ridge Associated Universities (ORAU) through a contract with NASA. The authors specially thank Dr. Matthias Steiner at NCAR, Dr. Ng Hok Kwan, Mr. Todd Farley, and Dr. Dallas Denery at NASA Ames Research Center for their invaluable peer reviews.

Appendix A

1) SGS TKE: Subgrid scale turbulent kinetic energy (SGS TKE) is turbulence-related variable that is only directly produced by the weather model. In the WRF model used, the Mellor-Yamada-Janjić (MYJ) planetary boundary layer (PBL) parameterization (Janjić 2002) predicts local vertical turbulent mixing not only in the PBL but also in the free atmosphere through the Mellor-Yamada level 2.5 turbulence closure model:

$$\begin{aligned} \frac{\partial q^2/2(x, y, z)}{\partial t} = & -\overline{u'w}(x, y, z) \frac{\partial U(x, y, z)}{\partial z} - \overline{u'w}(x, y, z) \frac{\partial V(x, y, z)}{\partial z} + \beta g \overline{\theta'_v w}(x, y, z) \\ & + \frac{\partial}{\partial z} \left(0.2 \ell q \frac{\partial q^2/2}{\partial z} \right) - \varepsilon. \end{aligned} \quad (A1)$$

$q^2/2$, u' , w , U , V , β , g , θ_v , l , and ε are the TKE, subgrid-scale u and w wind components, grid-resolvable U and V wind components, $\beta = 1/273$, gravity acceleration (9.8 m s^{-2}), virtual potential temperature, mixing length, and energy dissipation rate as a function of TKE and mixing length (l), respectively. Variables under the bar are subgrid-scale vertical momentum and heat fluxes that are parameterized in the ARW-WRF model.

2) FS EDR: The EDR ($\varepsilon^{1/3}$) at given grid point are estimated from second-order structure functions for u and v wind components along horizontal directions by assuming that the sensitivity to the universal structure functions in different NWP model is negligible in small-scales (Frehlich and Sharman 2004):

$$\varepsilon^{\frac{2}{3}}(x, y, z) = \frac{\langle \{q(x, y, z) - q(x, y, z + s)\}^2 \rangle}{C_q(s) D_{REF}(s)}. \quad (A2)$$

q is u and v wind components, and s , $C_q(s)$, and $D_{DEF}(s)$ are separation distance, correction function that takes into account NWP model spatial filter, and the reference structure function given by Lindborg (1999). $\langle \rangle$ bracket is the ensemble mean of four separation (s) options such as longitudinal u and v and meridional u and v wind components.

3) DEFSQ: Square of total deformation (DEF) that is sum of shear deformation and stretching deformation (Bluestein 1992).

$$DEF(x, y, z) = \left[\left\{ \frac{\partial V(x, y, z)}{\partial x} + \frac{\partial U(x, y, z)}{\partial y} \right\}^2 + \left\{ \frac{\partial U(x, y, z)}{\partial x} - \frac{\partial V(x, y, z)}{\partial y} \right\}^2 \right]^{\frac{1}{2}}. \quad (A3)$$

4) ADIV: Absolute value of horizontal divergence (DIV).

$$DIV(x, y, z) = \frac{\partial U(x, y, z)}{\partial x} + \frac{\partial V(x, y, z)}{\partial y}. \quad (A4)$$

5) VORTSQ: Square of vertical component of relative vorticity (VORT).

$$VORT(x, y, z) = \frac{\partial V(x, y, z)}{\partial x} - \frac{\partial U(x, y, z)}{\partial y}. \quad (A5)$$

6) ABW: Absolute value of vertical velocity.

$$ABW(x, y, z) = |w(x, y, z)|. \quad (A6)$$

7) F2D: Full 3-dimensional frontogenesis is simplified to 2-dimensional frontogenesis function (F2D) on p -coordinate using thermal-wind relation (Bluestein 1992).

$$F2D(x, y, z) = \{ \nabla_p \theta(x, y, z) \}^{-1} \left[- \left\{ \frac{\partial \theta(x, y, z)}{\partial x} \right\}^2 \left\{ \frac{\partial U(x, y, z)}{\partial x} \right\} - \left\{ \frac{\partial \theta(x, y, z)}{\partial y} \right\} \left\{ \frac{\partial \theta(x, y, z)}{\partial x} \right\} \left\{ \frac{\partial V(x, y, z)}{\partial x} \right\} - \left\{ \frac{\partial \theta(x, y, z)}{\partial x} \right\} \left\{ \frac{\partial \theta(x, y, z)}{\partial y} \right\} \left\{ \frac{\partial U(x, y, z)}{\partial y} \right\} - \left\{ \frac{\partial \theta(x, y, z)}{\partial y} \right\}^2 \left\{ \frac{\partial V(x, y, z)}{\partial y} \right\} \right]. \quad (A7)$$

Here, θ is potential temperature (K).

8) Brown1: Brown's index (Brown 1973) is a simplification of the original Richardson number tendency equation by Roach (1970) using thermal wind relation and assumption that the gradient wind is horizontal wind.

$$Brown1(x, y, z) = [0.3\{VORT(x, y, z) + f(x, y)\}^2 + DEF(x, y, z)^2]^{\frac{1}{2}}. \quad (A8)$$

Here, f is the Coriolis frequency.

9) NGM1: Multiplication of horizontal wind speed and total deformation were found to be the most skillful turbulence metric used in the NCEP's Nested Grid Model (NGM) output (Reap 1996).

$$NGM1(x, y, z) = \{U(x, y, z)^2 + V(x, y, z)^2\}^{1/2} \times DEF(x, y, z). \quad (A9)$$

10) HTG: Horizontal temperature gradient (HTG) is the deformation and vertical wind shear via the thermal-wind relation, which usually used by airlines (Buldovskii et al. 1976).

$$HTG(x, y, z) = \left[\left\{ \frac{\partial T(x, y, z)}{\partial x} \right\}^2 + \left\{ \frac{\partial T(x, y, z)}{\partial y} \right\}^2 \right]^{\frac{1}{2}}. \quad (A10)$$

Here, T is temperature ($^{\circ}\text{C}$).

Appendix B

Pontryagin's Minimum Principle (Bryson and Ho 1975) is applied to determine the control function for heading angle of aircraft that minimizes cost function (10) along optimal trajectory governed by Eqs. (6) and (7). The necessary condition for the control functions and the optimal trajectory is that there exist continuously differentiable Lagrange multipliers ($\lambda_{\phi}, \lambda_{\theta}$). The Hamiltonian is then,

$$H = C_t + C_r r(x, y, z) + \left(\frac{\partial \lambda}{\partial \phi} \right) \left\{ \frac{V_a \cos \psi(t) + U(\phi, \theta, z)}{R \cos \theta(t)} \right\} + \left(\frac{\partial \lambda}{\partial \theta} \right) \left\{ \frac{V_a \sin \psi + V(\phi, \theta, z)}{R} \right\}. \quad (B1)$$

So, the Euler-Lagrange equations are, as follows (B2), (B3), and (B4).

$$\begin{aligned} -\frac{d}{dt} \left(\frac{\partial \lambda}{\partial \phi} \right) &= \frac{\partial H}{\partial \phi} \\ &= \frac{\partial}{\partial \phi} \{C_r r(\phi, \theta, z)\} + \frac{1}{R \cos \theta(t)} \left(\frac{\partial \lambda}{\partial \phi} \right) \left\{ \frac{\partial}{\partial \phi} U(\phi, \theta, z) \right\} \\ &\quad + \frac{1}{R} \left(\frac{\partial \lambda}{\partial \theta} \right) \left\{ \frac{\partial}{\partial \phi} V(\phi, \theta, z) \right\}. \quad (B2) \end{aligned}$$

$$\begin{aligned} -\frac{d}{dt} \left(\frac{\partial \lambda}{\partial \theta} \right) &= \frac{\partial H}{\partial \theta} \\ &= \frac{\partial}{\partial \theta} \{C_r r(\phi, \theta, z)\} + \frac{1}{R \cos \theta(t)} \left(\frac{\partial \lambda}{\partial \phi} \right) \left\{ \frac{\partial}{\partial \theta} U(\phi, \theta, z) \right\} \\ &\quad + \left(\frac{\partial \lambda}{\partial \phi} \right) \frac{\tan \theta(t) \{V_a \cos \psi(t) + U(\phi, \theta, z)\}}{R \cos \theta(t)} + \frac{1}{R} \left(\frac{\partial \lambda}{\partial \theta} \right) \left\{ \frac{\partial}{\partial \theta} V(\phi, \theta, z) \right\}. \quad (B3) \end{aligned}$$

Under the condition that there is extremum for $t_0 \leq t \leq t_f$, the optimal heading angle satisfies,

$$\frac{\partial H}{\partial \psi} = 0 \rightarrow \tan \psi = \frac{\lambda_{\theta} \cos \theta}{\lambda_{\phi}}. \quad (B4)$$

And, for the necessary condition for optimality is $H(t_f) = 0$. So, the Lagrange multipliers are obtained when the Hamiltonian = 0, as follows.

$$\frac{\partial \lambda}{\partial \phi} = \frac{-\{C_t + C_r r(\phi, \theta, z)\} R \cos\psi(t) \cos\theta(t)}{V_a + U(\phi, \theta, z) \cos\psi(t) + V(\phi, \theta, z) \sin\psi(t)}. \quad (B5)$$

$$\frac{\partial \lambda}{\partial \theta} = \frac{-\{C_t + C_r r(\phi, \theta, z)\} R \sin\psi(t)}{V_a + U(\phi, \theta, z) \cos\psi(t) + V(\phi, \theta, z) \sin\psi(t)}. \quad (B6)$$

Differentiate in right and left hand sides of Eq. (B4) with respect to time, and Eqs. (B2), (B3), (B5), and (B6) are substituted,

$$\frac{d\psi(t)}{dt} = -\frac{\{F_{wind}(t) + F_{turb}(t)\}}{R \cos\theta(t) \{C_t + C_r r(\phi, \theta, z)\}}. \quad (B7)$$

where,

$$\begin{aligned} F_{wind}(t) &= -\sin\psi(t) \cos\psi(t) \frac{\partial U(\phi, \theta, z)}{\partial \phi} + \cos^2\psi(t) \sin\theta(t) U(\phi, \theta, z) \\ &+ \cos^2\psi(t) \cos\theta(t) \frac{\partial U(\phi, \theta, z)}{\partial \theta} - \frac{\partial V(\phi, \theta, z)}{\partial \phi} \\ &+ \sin\psi(t) \cos\psi(t) \sin\theta(t) V(\phi, \theta, z) + \cos\psi(t) \sin\psi(t) \cos\theta(t) \frac{\partial V(\phi, \theta, z)}{\partial \theta} \\ &+ V_a \cos\psi(t) \sin\theta(t) + \cos^2\psi(t) \frac{\partial V(\phi, \theta, z)}{\partial \phi}. \end{aligned}$$

$$\begin{aligned} F_{turb}(t) &= -\sin\psi(t) \cos\psi(t) \sin\theta(t) V(\phi, \theta, z) C_r r(\phi, \theta, z) \\ &+ \cos\theta(t) \cos\psi(t) \sin\psi(t) \frac{\partial V(\phi, \theta, z)}{\partial \theta} C_r r(\phi, \theta, z) \\ &- \cos\theta(t) \cos\psi(t) \sin\psi(t) V(\phi, \theta, z) C_r \frac{\partial r(\phi, \theta, z)}{\partial \theta} \\ &+ V_a \cos\psi(t) \sin\theta(t) C_r r(\phi, \theta, z) + V_a \sin\psi(t) C_r \frac{\partial r(\phi, \theta, z)}{\partial \phi} \\ &- \frac{\partial V(\phi, \theta, z)}{\partial \phi} C_r r(\phi, \theta, z) + V(\phi, \theta, z) C_r \frac{\partial r(\phi, \theta, z)}{\partial \phi} \\ &- \sin\psi(t) \cos\psi(t) \frac{\partial U(\phi, \theta, z)}{\partial \phi} C_r r(\phi, \theta, z) \\ &+ \sin\psi(t) \cos\psi(t) U(\phi, \theta, z) C_r \frac{\partial r(\phi, \theta, z)}{\partial \phi} \\ &+ \cos^2\psi(t) \sin\theta(t) U(\phi, \theta, z) C_r r(\phi, \theta, z) \\ &+ \cos^2\psi(t) \cos\theta(t) \frac{\partial U(\phi, \theta, z)}{\partial \theta} C_r r(\phi, \theta, z) - V_a \cos\theta(t) \cos\psi(t) C_r \frac{\partial r(\phi, \theta, z)}{\partial \theta} \\ &- \cos\theta(t) \cos^2\psi(t) U(\phi, \theta, z) C_r \frac{\partial r(\phi, \theta, z)}{\partial \theta} + \cos^2\psi(t) \frac{\partial V(\phi, \theta, z)}{\partial \phi} C_r r(\phi, \theta, z) \\ &- \cos^2\psi(t) V(\phi, \theta, z) C_r \frac{\partial r(\phi, \theta, z)}{\partial \phi}. \end{aligned}$$

In this study, $C_t = 1$, and $C_r = 1$ when the probabilistic SEATG at given grid point greater than 50% for MOG-level turbulence, while $C_r = 0$ when the SEATG is less than 50% for MOG-level turbulence at the given point.

References

- Bluestein, H. B., 1992: *Principles of Kinematics and Dynamics*. Vol. I. *Synoptic–Dynamic Meteorology in Midlatitudes*, Oxford University Press, 431 pp.
- Brown, R., 1973: New indices to locate clear-air turbulence. *Meteor. Mag.*, **102**, 347–360.
- Bryson, A. E., and Y. C. Ho, 1975: *Applied Optimal Control*, Taylor and Francis, Levittown, PA.
- Buldovskii, G. S., S. A. Bortnikov, and M. V. Rubinshtejn, 1976: Forecasting zones of intense turbulence in the upper troposphere. *Meteor. Gidrol.*, **2**, 9–18.
- Cornman, L. B., C. S. Morse, and G. Cuning, 1995: Real-time estimation of atmospheric turbulence severity from in-situ aircraft measurements. *J. Aircraft*, **32**, 171-177.
- DeLaura, R., and J. Evans, 2006: An Exploratory Study of Modeling En Route Pilot Convective Storm Flight Deviation Behavior, *Proceedings of the 12th Conference on Aviation, Range, and Aerospace Meteorology*, Atlanta.
- Frehlich, R., and R. Sharman, 2004: Estimates of turbulence from numerical weather prediction model output with applications to turbulence diagnosis and data assimilation, *Mon. Weather Rev.*, **132**, 2308–2324.
- Gill P. G., 2012: Objective verification of World Area Forecast Centre clear air turbulence forecasts. *Meteorol. Appl.* DOI:10.1002/met.1288.
- Gill PG, A. J. Stirling, 2012. Introducing convection to World Area Forecast Centre turbulence forecasts. *Meteorol. Appl.*
- International Civil Aviation Organization (ICAO), 2010: Meteorological service for international air navigation. – Annex 3 to the Convention on International Civil Aviation, 17th Edition, 206 pp. [Available online at <http://store1.icao.int/index.php/publications/annexes/3-meteorological-service-for-international-air-navigation.html>].
- Jardin, M. R., and A. E. Bryson, 2001: Neighboring optimal aircraft guidance in winds, *Journal of Guidance, Control, and Dynamics*, **24(4)**, 710–715.
- Jardin, M., and A. Bryson, 2012: Methods for computing minimum-time paths in strong winds, *Journal of Aircraft*, **35**, 165-171.
- Janjić, Z. I., 2002: Nonsingular implementation of the Mellor-Yamada level 2.5 scheme in the NCEP Meso model. *NCEP office note*, No. 437, 61 pp.
- Kim, J.-H., H.-Y. Chun, R. D. Sharman, and T. L. Keller: 2011: Evaluations of upper-level turbulence diagnostics performance using the Graphical Turbulence Guidance (GTG) system and pilot reports (PIREPs) over East Asia. *J. Appl. Meteor. Climatol.*, **50**, 1936-1951.
- Kim, J.-H., and H.-Y. Chun, 2010: A Numerical Study of Clear-Air Turbulence (CAT) encounters over South Korea on 2 April 2007. *J. Appl. Meteor. Climatol.*, **49**, 2381-2403.
- Kim, J.-H., and H.-Y. Chun, 2011: Statistics and possible sources of aviation turbulence over South Korea. *J. Appl. Meteor. Climatol.*, **50**, 311-324.
- Kim, J.-H., and H.-Y. Chun, 2012: A Numerical simulation of convectively induced turbulence above deep convection. *J. Appl. Meteor. Climatol.*, **51**, 1180-1200.
- Krozel, J., V. Klimenko, and R. D. Sharman, 2011: Analysis of clear-air turbulence avoidance maneuvers, *Air Traffic Control Quarterly*, **4**, 147-168.
- Lane, T. P., R. D. Sharman, S. B. Trier, R. G. Fovell, and J. K. Williams, 2012: Recent advances in the understanding of near-cloud turbulence. *Bull. Amer. Meteor. Soc.*, **93**, 499-515.
- Lester, P. F., 1994: *Turbulence: A New Perspective for Pilots*, Jeppesen, Co.
- Lindborg, E., 1999: Can the atmospheric kinetic energy spectrum be explained by two-dimensional turbulence? *J. Fluid Mech.*, **388**, 259–288.
- Lindborg, E. 2007: Horizontal wavenumber spectra of vertical vorticity and horizontal divergence in the upper troposphere and lower stratosphere, *J. Atmos. Sci.*, **64**, 1017–1025.
- McNally, D., K. Sheth, C. Gong, J. Love, C. H. Lee, S. Sahlman, and J. Cheng, 2012: Dynamic weather routes: a weather avoidance system for near-term trajectory-based operations, *28th International Congress of the Aeronautical Sciences (ICAS)*.

- Ng, H. K., B. Sridhar, S. Grabbe, and N. Chen, 2011: Cross-polar aircraft trajectory optimization and the potential climate impact. *30th Digital Avionics Systems Conference (DASC)*, Seattle, WA.
- Ng, H. K., B. Sridhar, and S. Grabbe, 2012: A practical approach for optimizing aircraft trajectories in winds. *31st Digital Avionics Systems Conference*, Williamsburg, Virginia, Institute of Electrical and Electronics Engineers.
- Ng, H. K., A. Morando, and S. Grabbe, 2010: Automated flight routing using stochastic dynamic programming, *Proceedings of the AIAA Aviation Technology, Integration, and Operations Conference*, Fort Worth, TX.
- Palopo, K., R. D. Windhorst, S. Suharwardy, and H.-T. Lee, 2010: Wind optimal routing in the national airspace system, *Journal of Aircraft*, **47**, 1584-1592.
- Roach, W. T., 1970: On the influence of synoptic development on the production of high level turbulence. *Quart. J. Roy. Meteor. Soc.*, **96**, 413-429.
- Skamarock, W. C. and J. B. Klemp, 2008: A time-split nonhydrostatic atmospheric model for weather research and forecasting applications. *J. Comput. Phys.*, **227**, 3465-3485.
- Trier, S. B., R. D. Sharman, R. G. Fovell, and R. G. Frehlich, 2010: Numerical simulation of radial cloud bands within the upper-level outflow of an observed mesoscale convective system. *J. Atmos. Sci.*, **67**, 2990-2999.
- Trier, S. B. and R. D. Sharman, 2009: Convection-permitting simulations of the environment supporting widespread turbulence within the upper-level outflow of a mesoscale convective system. *Mon. Wea. Rev.*, **137**, 1972-1990.
- Sharman, R. D., C. Tebaldi, G. Wiener, and J. Wolff, 2006: An integrated approach to mid- and upper-level turbulence forecasting. *Wea. Forecasting*, **21**, 268-287.
- Sharman, R. D., 2013: New developments in the Graphical Turbulence Guidance product, *Workshop on aviation turbulence*, Boulder, CO.
- Sridhar, B., H. K. Ng, and N. Y. Chen, Aircraft trajectory optimization and contrails avoidance in the presence of winds. *10th AIAA Aviation Technology, Integration, and Operations (ATIO) conference*, Fort Worth, TX, 13-15 Sep. 2010.
- Steiner M., R. Bateman, D. Megenhardt, Y. Liu, M. Pocerlich, and J. Krozel, 2010: Translation of ensemble weather forecasts into probabilistic air traffic capacity impact. *Air Traffic Control Quarterly*, **18(3)**, 229-254.